Numerical Prediction Approach of Cavitation Erosion based on 3D Simulation Flow

A. Bel Hadj Taher[†], H. Kanfoudi and R. Zgolli

Laboratory of Hydraulic and Environmental Modeling, National Engineering School of Tunis, University of Tunis ELMANAR, 1002 Tunis, Tunisia

†Corresponding Author Email: ahmed.belhadjtaher@enit.utm.tn

ABSTRACT

In industry, the phenomenon of cavitation erosion can reduce the lifetime of the components of hydraulic machines. In this article, we present a new numerical approach to predict the mechanical impact resulting from the implosion of a cloud of bubbles, based on an energy approach. The objective of this approach is to determine the main damage mechanisms and to estimate the intensity of the impact pressure near the surface. The large eddy simulation (LES) approach is coupled with a homogeneous cavitation model to assess the risk of erosion around the hydrofoil NACA0009. Indeed, three functions, namely the Pressure Intensity Function (PIF), the steam intensity function and the Erosive Power Function (EPF), are applied to assess the spatial distribution of eroded areas. The calculations show that the functions based on the pressure term are in good agreement with the experiments, namely: the PIF and EPF functions. On the other hand, we assume that the implosion of the cloud of bubbles produces a pressure wave, which in turn causes the implosion of small bubbles near the wall. Then the erosion will be the result of these secondary implosions and not of the cloud of bubbles. Therefore, we vary the degree of proximity of these micro-bubbles near the wall to choose either the shock wave or the micro-jet to extrapolate the pressure field. We can compare these estimates with the existing erosion measurements and we can conclude that the calculations respond more to the probability of the presence of a micro-jet than to the presence of a shock wave.

Keywords: Cavitation erosion; Shock wave; Micro-jet; 3D unsteady simulation; Ansys-CFX.

NOMENCLATURE

C_D	drag coefficient	U_∞	inlet flow velocity
C_L	lift coefficient	V_{vap}	vapor volume
C_p	pressure coefficient	α_v	vapor volume fraction
m^+	vaporization source term	μ_l	liquid viscosity
m^-	condensation source term	μ_v	vapor viscosity
P_∞	outlet pressure	ρ_l	liquid density
R_0	initial radius of bubble	ρ_v	vapor density
R_e	Reynolds number	γ	dimensionless distance

1. INTRODUCTION

The occurrence of hydrodynamic cavitation is very common in hydraulic devices, such as hydrofoils, centrifugal pumps, turbines and propellers. It occurs as a result of a sudden and rapid decrease in pressure in a flowing fluid (Liang *et al*. 2020; Ye *et al*. 2020). In order to numerically predict cavitation erosion, it is necessary to model the coupling between turbulence and cavitation (Ji *et al*. 2014; Cheng *et al*. 2020). The implosion of these cavities near the wall results in the formation of a high mechanical impact directed towards the material can cause material tearing. This phenomenon is called cavitation erosion. This harmful effect generates additional costs on the use of hydraulic devices. The evaluation of this risk becomes necessary and indispensable during the conception process. Usually, it is achieved by testing through prototypes. These methods are visual assessments of the cavity collapse phase using high-speed cameras followed by paint tests or acoustic measurements (Bark *et al*. 2004). These methods are very expensive and can be adopted after the

design phase. As a result, numerical methods offer the possibility of evaluating the risk of erosion from the design phase. They can reproduce the dynamics and the main characteristics of sheet cavity (Bensow, 2010).

Computer developments offer an opportunity for researchers to simulate different types of flows, such as bubble flows, turbulent cavitating flows, fluid-structure interaction, and flows in enclosures and channels. All the approaches presented in previous studies (Dular and Delgosha 2009; Arabnejad *et al.* 2020a,b; Li 2012; Peters *et al.* 2018; Usta and Korkut 2019) can be classified into two groups, namely: methods based on a compressible solver or an incompressible one.

For compressible simulation, the erosion evaluation is carried out by the force of the shock waves induced by the collapse phase. To predict this risk, Mihatsch *et al.* (2015) developed a numerical method to assess the risk of the cavitation occurrence in an axially symmetric nozzle. Koukouvinis *et al.* (2017) predicted eroded areas in diesel injectors. Blume and Skoda (2019) successfully predicted eroded areas by locating the positions of the pressure peaks on the hydrofoil surface. It should also be noted that these compressible methods have also been used for low-velocity cavity flows around foils and propellers (Arabnejad *et al.* 2020).

Based on incompressible simulation, several studies have been presented to estimate the mechanical impact. Ochiai *et al.* (2013) evaluated this risk based on the acoustic pressure of Lagrangian bubbles injected in a flowing fluid. Moreover, Peters and El Moctar (2020) adopted the same method in a multi-scale Euler-Lagrange simulation of cavitating flows. Krumenacker *et al.* (2014) developed a numerical approach, based on the Rayleigh-Plesset model, allowing the prediction of eroded zones from Eulerian simulation. Li *et al.* (2014) predicted the eroded areas around the hydrofoil based on the accumulation over time of the pressure derivative. Koukouvais *et al.* (2015) developed an erosive indicator to identify and assess eroded areas based on the pressure term. Dular and Delgosha (2009) developed a numerical method founded on the collapse of spherical bubbles near the wall. They estimated the mechanical impact intensity as a function of the jet velocity and the yield strength of the material considered. Peters *et al.* (2018) evaluated the impact risk through a numerical approach, considering that the implosion of micro-cavities near the solid surface is in the form of a micro-jet. They developed an indicator to qualitatively evaluate the erosion potential, founded on the number of impacts and their intensity on the impacted areas. To assess the risk of erosion, Lei *et al.* (2021) applied three methods, namely: the Intensity Function Method (IFM), the time-averaged aggressiveness indicators and the Gray Level Method (GLM). They suggested the use of the time-averaged pressure field to improve the accuracy of the GLM.

Adopting the energy approach, certain numerical methods have been proposed (Bark *et al.* 2004; Arabnejad *et al.* 2020) and applied (Fortes-patella *et al.* 2012; Vogel and Lauterborn 1988) in the literature to better characterize and assess the risk of cavitation erosion. This approach is based on the concept of an energy cascade between the macro-cavities, the micro-cavities and the damaged surface. The impact risk is related to the vapor content and the pressure when they collapse. According to Vogel and Lauterborn (1988), this pressure could be reasonably approximated by the pressure measured far from the center of the collapse. Thus, for complex unstable cavitating flows, defining this pressure was generally difficult. Bark *et al.* (2004) showed that when a cavity expanded in the region of low pressure, the surrounding liquid would gain potential energy. It would be transformed into kinetic energy if the implosion of the cavities took place in an area which was characterized by high pressure. At the end of the collapse phase, the kinetic energy of the liquid would be converted into acoustic energy, which was radiated in the form of pressure waves. It would alternately act as a water hammer or a micro jet against the material depending on the distance between the bubble center and the solid wall. Identifying the cause of erosion has presented a major difficulty for researchers. While some researchers like Peters *et al.* 2018, Peters *et al.* (2015) and Dular and Coutier-Delgosha (2009) made the micro-jet responsible for erosion, others like Fortes-Patella *et al.* (1998), Van Terwisga *et al.* (2009), Bark *et al.* (2004) and Li *et al.* (2016) believed that the overpressure wave emitted during a bubble implosion was the cause.

In this article, we present a numerical approach to assess the risk of cavitation erosion based on a 3D calculation of cavitating flows. Similar to Fortes-Patella *et al.* (1998), the present approach uses the energy cascade between the cavity collapse and the damaged surface to characterize and locate the mechanical impact. Thus, we propose a new erosive function in order to locate the impact zones. This function should be compared with other erosive functions presented in the literature. However, to assess the mechanical impact intensity, we present the impact pressures for both micro-jet and shock-wave cases. The approach is then applied to a flow around the NACA0009 hydrofoil, and the erosion model obtained by the present approach is confronted to the measurements of Arabnejad *et al.* (2018).

2. NUMERICAL METHODS

2.1 Governing equations

The conservation equations of mass and momentum for an incompressible fluid are given by Eq. (1) and Eq. (2) (Yuan *et al.* 2001):

$$\frac{\partial u_i}{\partial x_i} = 0 \qquad (1)$$

$$\frac{\partial u_i}{\partial t} + \frac{\partial (u_i u_i)}{\partial x_j} = -\frac{1}{\rho}\frac{\partial p}{\partial x_i} + \nu\frac{\partial^2 u_i}{\partial x_j \partial x_i} \qquad (2)$$

The instantaneous speed along the direction x, and the static pressure are represented respectively by the parameters u_i and p. The set of Eqs (1) and (2) forms a closed system capable of describing in detail the turbulent movement, including all fluctuations.

Laminar viscosity μ and density ρ are respectively defined (Yuan *et al.* 2001) as follows:

$$\mu = \alpha_v \mu_v + (1 - \alpha_v)\mu_l \qquad (3)$$

$$\rho = \alpha_v \rho_v + (1 - \alpha_v)\rho_l \qquad (4)$$

The application of the filter to Eqs. (1) and (2) gives the Large Eddy Simulation (LES) equations (Smagorinsky 1963):

$$\frac{\partial \overline{u_j}}{\partial x_j} = 0 \qquad (5)$$

$$\frac{\partial \overline{u_i}}{\partial t} + \frac{\partial (\overline{u_i u_j})}{\partial x_j} = -\frac{1}{\rho}\frac{\partial \overline{p}}{\partial x_i} + \frac{\partial}{\partial x_j}\left\{\nu\left(\frac{\partial \overline{u_i}}{\partial x_j} + \frac{\partial \overline{u_j}}{\partial x_i}\right) + \tau_{ij}^S\right\} \qquad (6)$$

The Sub-Grid Scale (SGS) stresses are as follows:

$$\tau_{ij}^S = \overline{u_i}\,\overline{u_j} - \overline{u_i u_j} \qquad (7)$$

Tensor τ_{ij}^S characterizes the action of unresolved velocity fluctuations, acting as a stress that needs to be modeled:

$$\tau_{ij}^S = 2\nu_t \overline{S}_{ij} \qquad (8)$$

where ν_t represents the turbulent viscosity at the scale of the sub-grid, and S_{ij} represents the strain rate tensor which is given by Eq. (9):

$$\overline{S}_{ij} = \frac{1}{2}\left(\frac{\partial \overline{u_i}}{\partial x_j} + \frac{\partial \overline{u_j}}{\partial x_i}\right) \qquad (9)$$

Closing ν_t is determined by the LES wall-adapting local Eddy-viscosity model (Nicoud and Ducros 1999).

2.2 Physical cavitation model

The cavitation model used in this article is based on the transport equation of α_v with source terms, which is given by Eq. (10). (For more details, please see the thesis of Kanfoudi 2012).

$$\frac{\partial (\rho_v \alpha_v)}{\partial t} + \frac{\partial (\rho_v \alpha_v u_i)}{\partial x_i} = m^+ - m^- \qquad (10)$$

where α_v represents the volume fraction of vapor, and m^- and m^+ respectively represent the mass transfer rates for the condensation and vaporization processes (Kanfoudi 2012). They are defined as:

$$m^+ = C_e \alpha_v^{\frac{2}{3}}(1 - \alpha_v)^{\frac{4}{3}}\frac{\rho_v \rho_l}{\rho_m}\sqrt{\frac{2}{3}\frac{p_v - p}{\rho_l}} \qquad (11)$$

$$m^- = C_c \alpha_v^{\frac{1}{6}}(1 - \alpha_v)^2 \frac{\rho_v \rho_l}{\rho_m}\sqrt{\frac{2}{3}\frac{p - p_v}{\rho_l}}$$

with

$$\begin{aligned} C_c &= -10 R_0^{\frac{3}{2}} n_0^{\frac{5}{6}} \\ C_e &= 5\sqrt[3]{n_0} \end{aligned} \qquad (12)$$

where n_0 represents the concentration of nucleation, and R_0 represents the initial radius of the vapor bubbles. The equation of α_v is given by Eq. (13) (Yuan *et al.* 2001):

$$\alpha_v = \frac{n_0 \frac{4}{3}\pi R^3}{1 + n_0 \frac{4}{3}\pi R^3} \qquad (13)$$

The values of these quantities are respectively: 10^{-6} m and 5.10^{14} *nucleations/m³* (Kanfoudi 2012).

2.3 Numerical approach proposed for modeling the mechanical impact

We illustrate in Fig. 1 a descriptive schema describing the suggested numerical approach. This scenario makes it possible to define the energy transfer from the macroscopic cavity to the impact area.
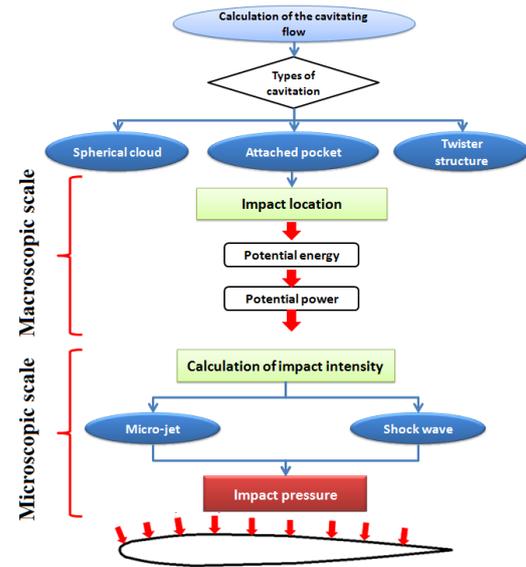

Fig. 1. Descriptive schema of proposed approach.

The consensus of this approach is that the collapse of macro-cavities cannot directly damage the material, because the energy is not sufficiently concentrated. In fact, the potential energy stored in a macroscopic cavity is first converted into an acoustic wave, and then into erosive power in the microscopic cavities. Two impact structures describe the final stages of the life of a micro-cavity, either the propagation of a shock wave or the formation of a micro-jet. These two structures interact with solid surfaces, causing property damage. To assess the intensity of the mechanical impact, we can estimate its impact pressure.

2.3.1. Characterization and location of mechanical impact

For any type of cavitation, the potential energy characterizing the implosion phase will be evaluated according to Eq. (14), also adopted by Fortes-Patella (1998) and Bark *et al.* (2004):

$$E_{pot} = \Delta p . V_{vap} \tag{14}$$

where $\Delta p = (p - p_{vap})$ is the difference between the pressure p and the saturation vapor pressure p_{vap}, and V_{vap} is the vapor volume. The intensity of the impact depends on the rate of transfer of potential energy to potential power. The latter is determined as the particle derivative of the potential energy.

$$P_{pot} = \frac{dE_{pot}}{dt} = \Delta p . \frac{dV_{vap}}{dt} + \frac{dp}{dt} . V_{vap} \tag{15}$$

Furthermore, the potential power density is reformulated by Eq. (16):

$$\frac{P_{pot}}{V_{cell}} = \underbrace{\Delta p . \frac{d\alpha}{dt}}_{(1)} + \underbrace{\frac{dp}{dt} . \alpha}_{(2)} \tag{16}$$

where $\alpha = V_{vap} / V_{cell}$. The particle derivatives in Eulerian writing of the vapor volume fraction and the pressure depend on time and space and can be written as follows:

$$\frac{d\alpha}{dt} = \frac{\partial\alpha}{\partial t} + \vec{v} . \nabla\alpha \text{ and } \frac{dp}{dt} = \frac{\partial p}{\partial t} + \vec{v} . \nabla p \tag{17}$$

We propose to evaluate the potential power distribution according to the order of the magnitude of the two terms (1) and (2) in Eq. (16).
Neglecting term (1) for term (2), the density will be represented by the Pressure Intensity Function (PIF), adopted also by Li *et al.* (2014).

$$PIF = \alpha \frac{dp}{dt} \tag{18}$$

The impact can only occur if the PIF crosses threshold S_{e1}, $PIF > S_{e1}$.

Neglecting term (2) for term (1), the density will be represented by the Vapor Intensity Function (VIF), adopted as well by Fortes-Patella and Reboud (1998) and Usta and Korkut (2019).

$$VIF = \left(\frac{d\alpha}{dt}\right)(p - p_v) \tag{19}$$

Like the first function, the impact can only occur if the VIF exceeds a threshold value S_{e2}, $VIF > S_{e2}$.

We put forward a new function that considers both terms (1) and (2) at the same time. Accordingly, the function representing the potential power density will be given by the Erosive Power Function (EPF).

$$EPF = \frac{P_{pot}}{V_{cell}} = (PIF + VIF) = (p - p_v)\left(\frac{d\alpha}{dt}\right) + \alpha\left(\frac{dp}{dt}\right) \tag{20}$$

The impact can only occur if the EPF exceeds a threshold value S_{e3}, $EPF > S_{e3}$.

The PIF, the VIF and the EPF are applied individually to the hydrofoil surface. These functions are evaluated at each time step. When the simulation converges and reaches the predicted physical time, the values of these functions are ready to be used to characterize and identify the impact location.

Due to the lack of knowledge on the surface of the hydrofoil, we apply a variety of thresholds to the previous functions to evaluate their distribution. The sensitivity test of the threshold values must respect the following properties:

- The different cavitation types must be captured.

- A minimum threshold must be respected to eliminate the high impact risk on the entire surface of the hydrofoil.

2.3.2. Evaluation of intensity of mechanical impact

The collapse of a macroscopic vapor cavity cannot damage the material, but it is rather the transfer of energy from the macroscopic cavity to the damaged surface. The last phase of a bubble life can be defined by two impact structures, namely:

a) Mechanical impact in form of micro-jet

The formation process of the mechanical impact follows very complex steps:

The propagation of the shock wave towards the bubbles near the solid surface is explained by the collapse of the cavitation cloud. The effect of this wave causes the birth of the high-speed micro-jet phenomenon, which serves to damage the surface of the profile.

The impact of this micro-jet causes a very short duration pressure, called the water hammer pressure, which is defined as the impact pressure in this paper. This pressure corresponding to an impact velocity of several hundred meters per second is greater than the yield strength of metallic materials.

Plesset and Chapman (1971) estimated the micro-jet velocity by Eq. (21):

$$V_{jet} = 8.97\gamma^2 \sqrt{\frac{P_{collapse}}{\rho_l}} = 8.97\gamma^2 \sqrt{\frac{|p - p_v|}{\rho_l}} \tag{21}$$

where $\gamma = h/R_0$ characterizes the dimensionless distance between the micro-cavities (bubbles) and the surface of the profile, R_0 is its initial diameter, and h is its distance from the surface. The micro-jet velocity is an essential parameter for calculating the impact pressure.

$$P_{impact} = c . \rho_l . V_{jet} \tag{22}$$

where c is the velocity of the sound in water.

b) Mechanical impact in form of shock wave

At the end of the final phase of the collapse, we assume that the rapidly increasing vapor pressure in the bubble will overcome the inertia of the liquid in the form of a spherical and symmetrical shock wave.

This allows us to adopt the model of Rayleigh (1917), which shows that the local pressure undergoes an increase at the end of the collapse of the spherical bubble. This model is only applied for the case of spherical bubbles, and therefore for distances very close to the solid wall.

The pressure field can be determined from Eq. (23) (Franc and Michel 2004).

$$\frac{p(r,t) - p_\infty(t)}{\rho_l} = \ddot{R}\frac{R^2}{r} + 2\dot{R}^2\left[\frac{R}{r} - \frac{R^4}{4r^4}\right] \quad (23)$$

where $\dot{R}$ is known from Eq. (24), and $\ddot{R}$ can be deduced by derivation.

$$\dot{R} = -\sqrt{\left(\frac{2}{3}\frac{p_\infty - p_v}{\rho_l}\right)\left[\frac{R_0^3}{R^3} - 1\right]} \quad (24)$$

$$\ddot{R} = -\left(\frac{p_\infty - p_v}{\rho_l}\right)\left(\frac{R_0^3}{R^4}\right) \quad (25)$$

Indeed, the impact pressure is given by Eq. (26):

$$p_{impact} = \left[\frac{R}{3r}\left[\frac{R_0^3}{R^3} - 4\right] - \frac{R^4}{3r^4}\left[\frac{R_0^3}{R^3} - 1\right] \times (p_\infty - p_v)\right] + p_\infty \quad (26)$$

Below $\delta = R/R_0 = 0.63$, the behavior of the dimensionless pressure exhibits a maximum in the liquid. Hence, the maximum pressure of a shock wave is:

$$p_{impact-max} = \left[\frac{\left[\frac{R_0^3}{4R^3} - 1\right]^{4/3}}{\left[\frac{R_0^3}{R^3} - 1\right]^{1/3}} \times (p_\infty - p_v)\right] + p_\infty \quad (27)$$

The maximum amplitude of this parameter is very influenced by the value of δ.

Moreover, it occurs at a distance of:

$$\frac{r_{max}}{R} = \left[\frac{\frac{R_0^3}{R^3} - 1}{\frac{R_0^3}{4R^3} - 1}\right]^{1/3} \quad (28)$$

In this model, only the pressure and the inertial forces are taken into account after the bubble implosion. Thus, the propagation of the pressure wave is the effect of these inertial forces.

In this study, we assume that the bubbles will collapse in a spherical form, regardless of its distance from the solid wall.

3. RESULTS AND DISCUSSIONS

3.1 Validation of numerical approach for simulating the cavitation around NACA 0009

3.1.1. Simulation configuration

In this article, we use the Ansys-CFX code, with an incompressible solver.

Three-dimensional numerical simulation is run around the hydrofoil NACA0009 to assess the dynamics of the unsteady cavitating flow. As an initial condition, we use a steady cavitating flow field to progress the calculation of the sheet cavity.

The hydrofoil cord is *c=100 mm* with an angle of incidence of 5° to the flow direction, as depicted in Fig. 2.

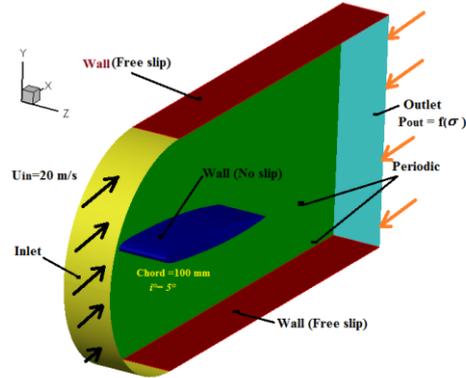**Fig. 2. NACA009 3D geometry.**

A velocity equal to $U_{inlet}=20$ *m/s* and a static pressure determined according to the number of cavitation $\sigma=1.2$ are applied respectively at the inlet and at outlet of the computation domain.

$$\sigma = \frac{p_{out} - p_v}{\frac{1}{2}\rho_l U_{in}^2} \quad (29)$$

The Reynolds number can be expressed by:

$\text{Re} = \rho_l U_{inlet} c / \mu_l$. In this simulation, the Reynolds number is 2.10^6. Thus, the flow regime is turbulent.

For the numerical calculation, we set the time interval to 10^{-5} s according to the number of the Courant-Friedrichs-Lewy, which is set to 0.5. For more precision of numerical results, the convergence criteria adopt the RMS residual type with a residual target of 10^{-5}.

Automatic processing is adopted near the wall to better model the boundary layer, more precisely the viscous sub-layer (Menter 1994). To numerically capture the boundary layer, a value of $y+=1$ is fixed. Fig. 3. shows the grid spacing near the wall.

Table 1 gathers the properties of fluids as well as the boundary conditions for the hydrodynamic validation.

To study the sensitivity of the numerical solution of drag and lift coefficients with respect to the number of nodes, we test three mesh types, as provided in Table 2. The lift and drag coefficients are given by Eq. (30):

$$C_L = \frac{lift}{\frac{1}{2}\rho_l U_{in}^2 c} \ ; C_D = \frac{Drag}{\frac{1}{2}\rho_l U_{in}^2 c} \quad (30)$$
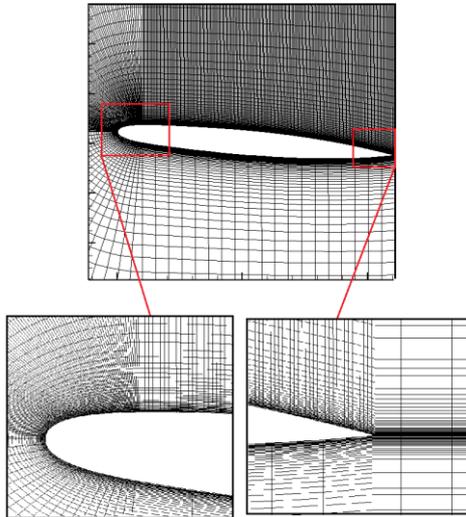
Fig. 3. Adopted mesh.

Table 1 Fluid properties and boundary conditions for numerical simulation.

Boundary conditions	NACA0009 *(AoA= 5 deg)*	
Flow velocity	$U_{in} = 20 m/s$	
Cavitation number	$\sigma = 1.2$	
Outlet pressure	$P_{out} = 242.5 kPa$	
Chord	C= 0.100m	
Turbulent intensity (%)	1	
Foil	No-slip wall	
Mid-span	Periodic	
Tunnel walls (top and bottom)	Slip wall	
Fluid properties (T = 25 °C)	Vapor	Liquid
Density (kg/m³)	0.023	997
Vapor pressure (kPa)	3.166	

We present in Table 2 the results of the calculated lift and drag coefficients. We notice that the results which correspond to the meshes M1 and M2 are nearly similar. Therefore, we adopt the medium-resolution mesh for the unsteady cavitation simulation, which is based on the study of Kanfoudi *et al.* (2017).

3.1.2. Unstable flow validation

The aim of presenting unsteady calculations with the LES approach is to study and analyze the dynamics of the detachment of the sheet cavity. To validate the model, we compare the numerical results with the measurements of Ait bouziad (2006).

To better detect the evolution of the sheet cavity detachment as well as the unstable cavitating flow, we use as a practical parameter the volume of vapor, and its expression is given as follows:

$$V_{vap} = \frac{1}{c} \sum_{i=1}^{N} \alpha_i V_i \qquad (31)$$

where α_i represents the volume fraction of vapor, N and V_i respectively denote the number and volume of control volumes presented in the calculation domain.

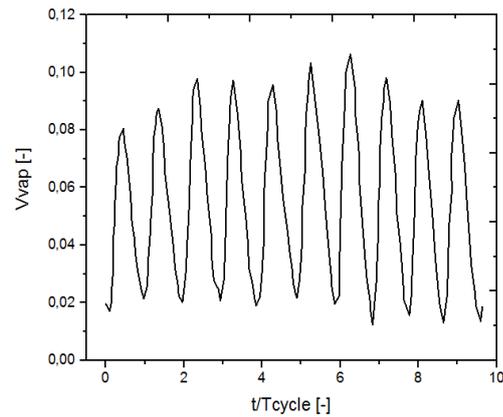We present in Fig. 4 10 typical cycles of the vapor volume.

Fig. 4. Cycles of unstable sheet cavity (Kanfoudi *et al.* 2017).

In order to evaluate the sheet cavity dynamics, we illustrate in Fig. 5 a life cycle of a sheet cavity around the NACA0009 profile. We focus on 10 typical moments. The period of the cycle is *T_cycle = 0.008 s*, and the frequency of the cycle is *f_cycle=122 Hz* with *Stc = 0.61*.

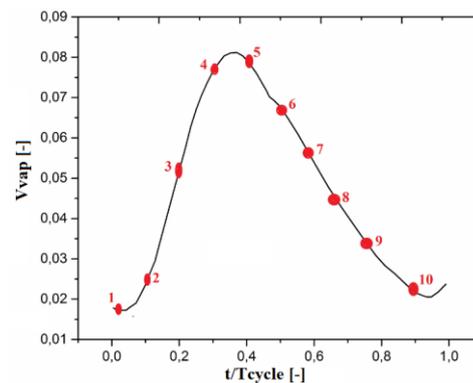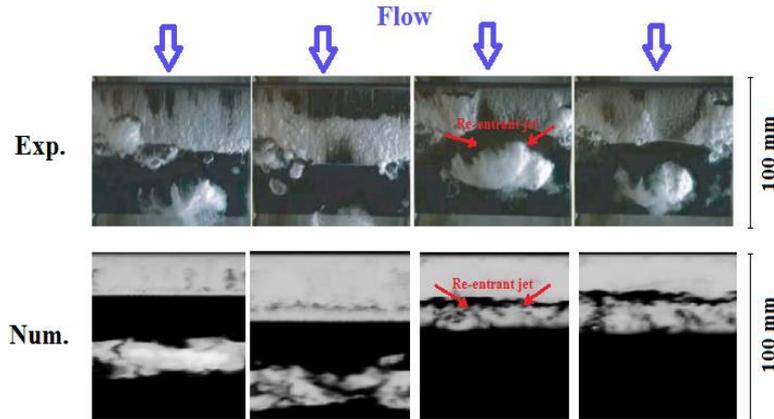**Fig. 5. Evolution of vapor volume during a single cycle.**

Table 1 Mesh independence test (Kanfoudi *et al.* 2017)

	Mesh resolution	Cells	C_L	C_D
M1	Fine	792 000	0.20177	0.0324
M2	Medium	588 294	0.20170	0.0322
M3	Coarse	385 000	0.19210	0.0298

Fig. 6. Experimental and numerical visualization of sheet cavity around NACA009 (experimental visualization given by Ait Bouziad 2006).

We present in Fig. 6. a qualitative comparison between the temporal evolution of the numerical and experimental unstable cavitating flows around NACA0009 for $\sigma=1.2$. The sheet cavity is very unstable with large transient cavities detaching almost cyclically. The rupture of the main cavity causes the appearance of small transient cavities, which will be transported by the flow towards the trailing edge where they collapse. If the length of the main cavity reaches a maximum value, the transient generation process of the cavity begins again. During the growth of the main cavity, a re-entrant jet is produced, which passes under the main cavity towards the upstream of its detachment point. The appearance of the re-entrant jet takes place at the point of stagnation between the closing of the mobile cavity and the transient cavity in the process of disappearing. The different phases of the life cycle of the cavitating structure are well modeled and captured by the numerical model. The calculations depicted in Fig. 6. are qualitatively similar to the experimental measurements.

To characterize the sheet cavity detachment mechanism, a temporal distribution of the pressure gradient in the *x* direction as a function of the sheet cavity dynamics is presented in Fig. 7.

At instant T1, a negative pressure gradient appears at the leading edge of the hydrofoil, which causes a depression on the upper surface, allowing the development of the sheet cavity. The convection and the passage of the small cavities of the previous cycle from the leading edge to the trailing edge are justified by the predominance of the negative pressure gradient.

Due to the pressure of the liquid, the vapor cavity collapses at the trailing edge and continues to grow to its maximum length and becomes thicker (T2 and T4).

Flow separation begins to occur in the closure region of the main sheet cavity as soon as it becomes thicker. This is explained by the positive pressure gradient at the tip of the sheet cavity which promotes the development of an inward jet and also

the formation of small vortex structures in the region of the vapor pocket closure (T5 and T6).
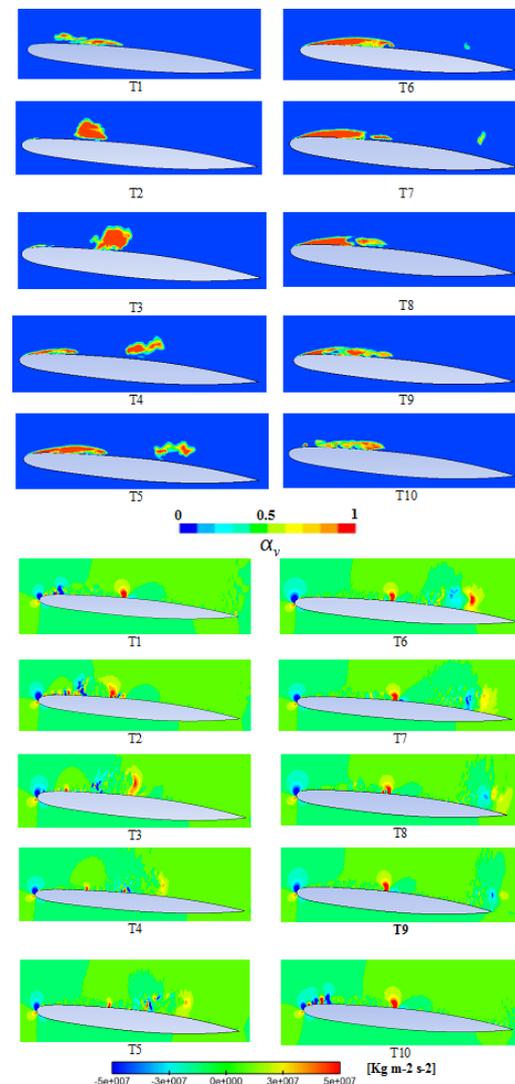
Fig. 7. Time evolution of cavitation shedding and pressure gradient on x direction for one cycle.

The observed pressure gradient between times T6 and T8 is explained by the formation of the reentering jet, which moves upstream along the hydrofoil surface. This phenomenon provokes the rupture of the interface located between the cavitating structure and the surface of the profile. It divides the main steam cavity into small secondary cavities (T6 to T8). After the detachment of the sheet cavity, the disappearance of vapor is noticed at the leading edge and a new sheet cavity begins to develop (T9 and T10). At these instants, a positive pressure gradient is observed just at the time of the collapse of the cavitating structures.

To evaluate the mechanical impact intensity, we propose to calculate the impact pressures for both impact structures (shock wave and micro-jet). Indeed, the calculation of the impact pressure is based on the pressure oscillations on the profile surface.

The interest behind this presentation is essentially qualitative, both to show the ability of the model to detect and to predict pressure waves.

It should be noted that these functions do not depend either on the cavitation model or on the numerical approach.

The calculated pressure oscillations for the different positions are presented in Fig. 8. We note that the suggested cavitation model is able to adequately predict pressure wave oscillations. The observed pressure peaks cannot generate damage, but they can carry enough energy to trigger other events, namely: micro-jet formation and shock wave propagation.
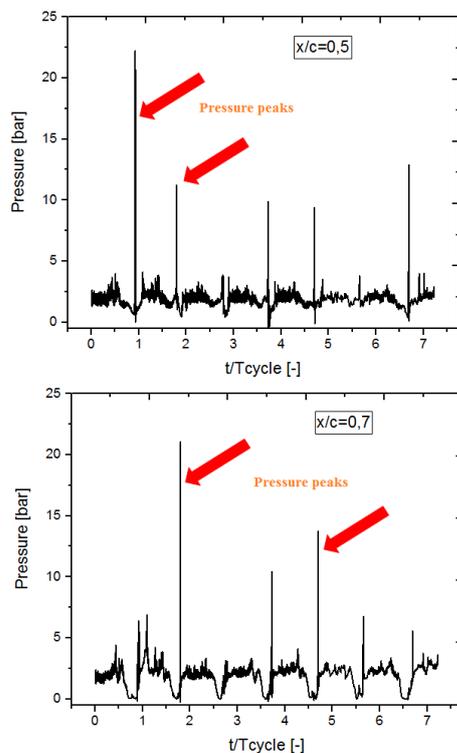
Fig. 8. Visualization of pressure oscillations at two positions.

3.2 Prediction of mechanical impact around NACA0009

3.2.1. Prediction of spatial distribution of impacted areas

While developing, the jet splits into two parts. The first part follows the main flow direction and the second part enters the cavity and moves towards the leading edge (this is the reentrant jet). The latter rotates upwards, separating the main attached pocket. This also involves a mechanical impact that is directed towards the wall.

The distributions of the PIF, the VIF and the EPF for the "cavitation cloud separation" form are illustrated in Fig. 9.

The damaged regions, which are associated with the collapse of this type of cavitation, are successfully captured by the erosive functions.

The spectral analysis of the function shows that the red areas correspond to regions of a high erosion intensity, while the green regions show regions of a low erosion intensity. The blue regions represent non-eroded areas.

The objective of this calculation is to identify the eroded areas through the PIF, the VIF and the EPF. The impacted and eroded zones obtained with the three proposed functions are shown in Fig. 10 (a), Fig.10 (b) and Fig. (c). It is indicated that the results found are highly influenced by the chosen threshold value. If this value is not correctly defined, we risk losing the results. To validate the suggested numerical approach, the calculations are compared with the measurements carried out by Arabnejad *et al.* (2018).

The distributions of the PIF and EPF functions calculated with the respective threshold values of $1e^{+09}$ and $1e^{+08}$ better correspond to the observed damaged regions, as shown in Fig. 10 (a) and Fig.10 (c). The eroded areas, caused by the collapse of the main pocket and its substructures, are indicated by the white rectangle. The eroded areas, related to the collapse of the horseshoe cloud cavity, are indicated at the trailing edge by a white ellipse.

The VIF calculated with the threshold of a $1e^{+07}$ value appears to be better correlated with the damage observed, as depicted in Fig. 10 (b).

Outside the leading-edge region, the damaged area caused by the collapse of the small cavities and the horseshoe structure and the separation from the main cavity are not captured by the VIF, due to defined thresholds. We notice that the VIF only detects large-scale changes in the vapor fraction and indicates the areas covered by the leaf cavity. It is suitable only for cavities with a stable behavior.

Compared with the measured damage, the pressure-related term of the PIF is the basis for the erosion process. The VIF is unreliable, particularly at the back of the profile. The EPF can capture eroded areas over the entire hydrofoil surface (at the leading edge, the center and the trailing edge). It
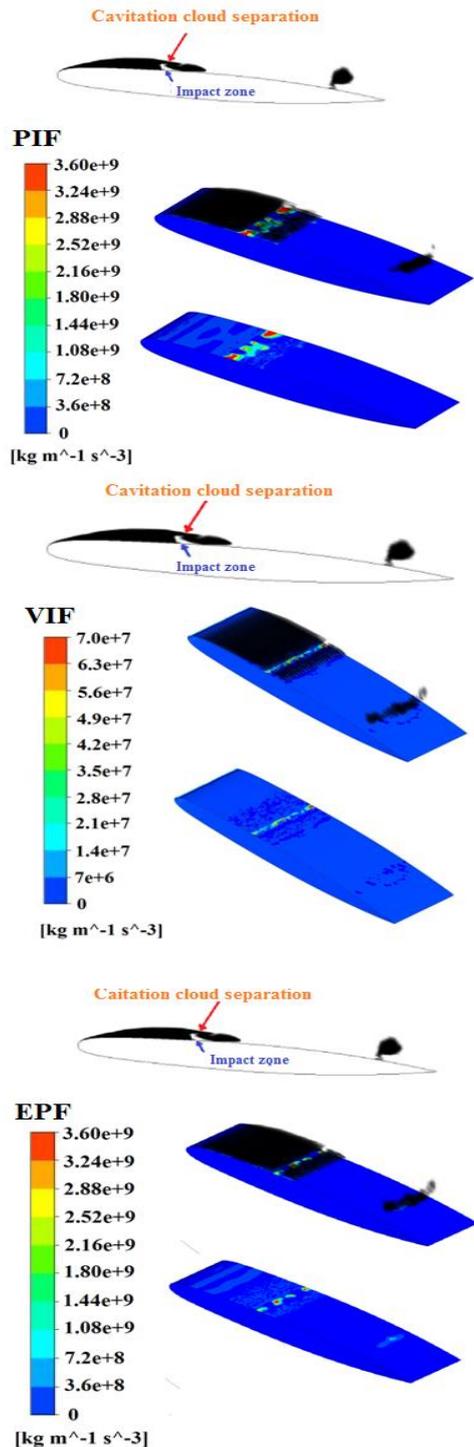
PIF

[kg m^-1 s^-3]

VIF

[kg m^-1 s^-3]

EPF

[kg m^-1 s^-3]

Fig. 9. Distribution of PIF, VIF, and EPF for "cavitation cloud separation" type around NACA0009 hydrofoil, U_{inlet} =12 m/s and σ=1.2.

provides an effective way to highlight the risk of the cavitation impact.

3.2.2. Impact intensity evaluation

The intensity of the impact, generated by the presence of the micro-jet is highly influenced by a dimensionless parameter. We therefore proceed to study the sensitivity of the intensity of the impact at
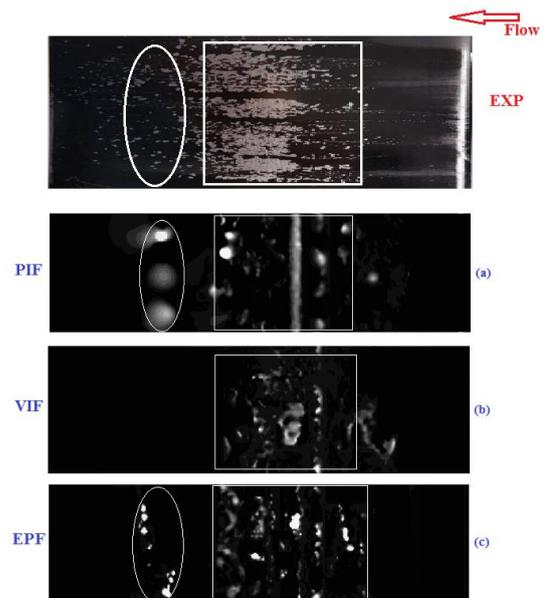

Fig. 10. Comparison between numerical results of three functions: (a) PIF with threshold value of 1e^+09 (b); VIF with threshold value of 1e^+07; (c) EPF with threshold value of 1e^+08 and damaged area obtained from paint test (experimental data from Arabnejad *et al*. 2018).

this distance. Two values of γ =0.75 and γ = 1.1 are tested. The choice of these values is based on the tests conducted by Tomita and Shima (1986). These value show that if the value is between 0.5 and 1, the impact will be caused by the micro-jet; while outside this range of values, the impact will result from the shock waves. In addition, for these values of γ, the shape of the bubble always remains spherical.

For a micro-jet, a dimensionless parameter δ, related to the critical size of the micro-cavity at the time of implosion, must be defined. A series of sensitivity tests allow us to fix this parameter at $\delta=R/R_0=0.1$.

We present in Fig. 11 the visualization of the impact pressure oscillations for the two impact structures. The impact pressure is calculated at two positions (x/c=0.5; 0.7).

We find that parameter γ has a great effect on the intensity of the mechanical impact. Furthermore, we notice that there is an overestimation of the impact amplitude of the case of the shock wave. This is justified by the assumptions adopted by the Rayleigh model that neglects the effect of viscosity, surface tension and gas content.

The Rayleigh model is used to estimate the pressure field and it relies on the assumption of an incompressible fluid, while the detection of the shock waves requires a model that relies on the assumption of a compressible fluid, namely: the model based on the Equation Of State (EOS). Despite this constraint, the adopted cavitation model can detect pressure waves, which in turn

x/c=0.5   x/c=0.7
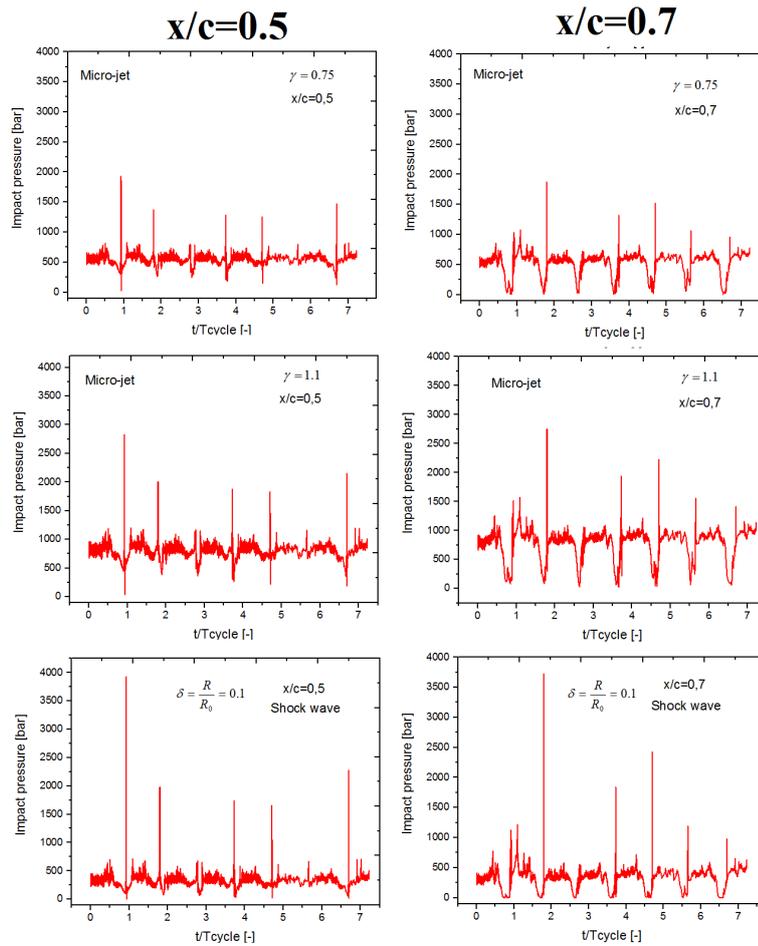
Fig. 11. Evolution of impact pressure for different impact structures.

carry enough energy to trigger other events, namely micro-jet formation or shock wave propagation. The ability of this model to detect pressure waves is related to the technique used to calculate the volume fraction of vapor, which is based on two calculation steps.

- In the first step, it determines the volume fraction of vapor.

- The second step consists in injecting the volume fraction of vapor resulting from the first calculations into the source term. Once the source term is fixed, the final vapor volume fraction is estimated using the transport equation. This approach will correct the interface tracking method.

In fact, the bubble contains non-condensable gas, which increases the pressure inside the bubble considerably at the end of implosion. It is precisely this increase in pressure which is at the origin of the rebound. Of course, the non-condensable gas content, which plays an undeniable role in the implosion process of a cavitation bubble, is a very difficult parameter to take into account. For this reason, we adopt the Rayleigh model, which neglects this parameter, to estimate the impact pressure in the vicinity of the solid wall. However,

because of this assumption, the pressure is largely overestimated compared to the micro-jet results.

Furthermore, this model is only valid for spherical collapses. Indeed, when the bubble is significantly deformed, the use of the Rayleigh model is very limited. Thus, all the calculations made in this article respond more to the probability of the micro-jet presence rather than the shock-wave presence.

3.3   Application cases

In this application, we consider that the surface of the hydrofoil is copper with a purity of (99.9%) and that it responds as a perfectly rigid solid until a critical limit is reached (elasticity limit P_y). Beyond this limit, the impacted zone follows the plastic deformation law. Therefore, its deformation is carried out only if the impact pressure exceeds a limit value. This condition is characterized by the critical velocity developed by Lush (1983). This velocity is expressed by:

$$V_{crit} = \sqrt{\frac{P_y}{\rho_l}\left(1 - \left(1 + \frac{P_y}{B}\right)^{-1/n}\right)} \qquad (32)$$

where $P_y = 200 MPa$ is the elastic limit of copper, with $B = 300 MPa$ and $n = 7$.

The formula of the limit pressure denoted by $P_{critical}$ can be given by Eq. (33):

$$p_{critical} = c.\rho_l.V_{crit} \tag{33}$$

Thus, the critical pressure is equal to:

$$p_{crit} = 1751 bar \tag{34}$$

To better assess the surface damage rate, we introduce a new parameter called I_{impact}, as the ratio between the impact and critical pressures.

$$I_{impact} = \frac{p_{impact}}{p_{critical}} \tag{35}$$

The mechanical impact can only cause damage if $I_{impact} > 1$.

The impact indicator during period T is presented by Eq. (36):

$$I_R = \sum_{t=0}^{T} I_{impact} \quad with \quad \begin{cases} I_{impact} = \dfrac{P_{impact}}{P_{critical}} & if \quad P_{impact} \succ P_{critical} \\ I_{impact} = 0 & if \quad P_{impact} \prec P_{critical} \end{cases} \tag{36}$$

The critical pressure is added to the impact pressure graphs to identify the impact times and intensities (See Fig. 12). We find that the impact structure and parameter γ have a large effect on the impact frequency and intensity.

We present in Fig. 13 a confrontation between the span-wise average of the measured damaged area and the numerical impact indicator after ten cycles of exposure to the cavitation flow. The results show that the damaged areas are located in the middle of the hydrofoil, which is explained by the increased impact frequency. A comparison with the measurements of Arabnejad *et al.* (2018) validates the proposed approach.

We find that the numerical model predicts the amplitude as well as the extent of damage with a minimal error. Unlike the downstream extent, the maximum damage amplitude is well modeled and predicted.

It appears that the numerical model concentrates the impact and damages on a larger region than the experimental measurement. The total distribution of the measured damage is concentrated in a radial position of 25 to 70 mm. On the other hand, simulation predicts damage over a distance of about 22 to 80 mm. A shift between the measured damage and the calculated one can also be observed in the rear part of the hydrofoil. Since this offset is constant (the predicted maximum occurs about 10 mm downstream of the measured one). This may be related to cavitation modeling. Despite these encouraging results, the calculation of the impact pressure for the shock wave case is only obtained with simplifying assumptions, which leads to the limitation of the use of the Rayleigh model. Thus, the performed calculations respond more to the probability of the presence of a micro-jet than to the presence of a shock wave.
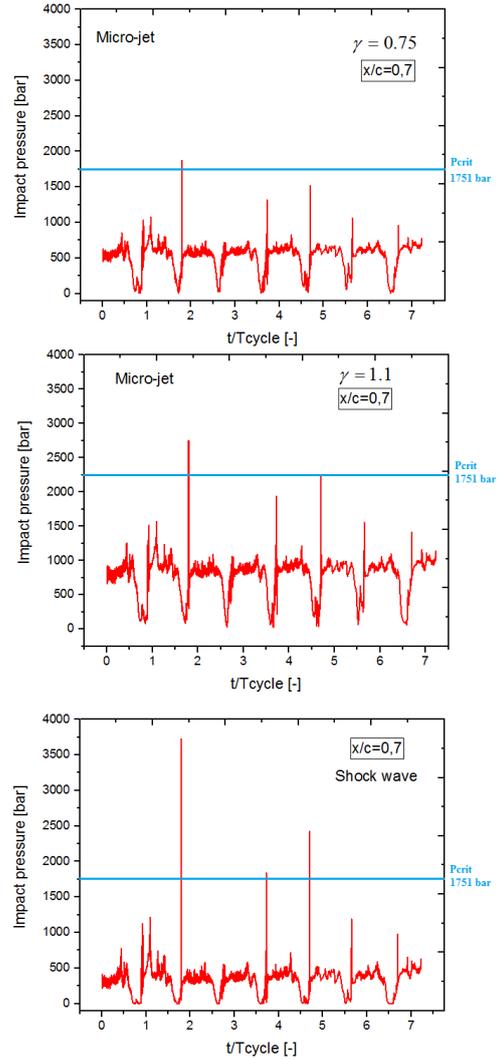
Fig. 12. Evolution of impact pressure compared to critical pressure.
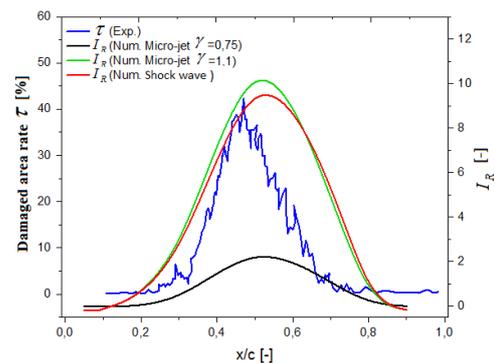
Fig. 13. Comparison between a) left scale: span-wise average of measured damaged area and b); right scale: numerical impact indicator (experimental data from Arabnejad *et al.* 2018).

4. CONCLUSION

We have proposed in this article a new approach to assess the erosion risk using incompressible

simulation of cavitating flows. This approach has been based on the energy cascade between the macroscopic cavities and the impacted material. In this approach, the potential energy contained in these cavities has been used to characterize the erosion risk using three erosive functions. The developed approach has then estimated how this potential energy is transferred to the solid surface through two impact mechanisms, namely: micro-jets and shock waves. To validate the numerical approach, we have compared the simulation of the cavitating flow around profile NACA0009 with the experimental data of Arabnejad *et al*. (2018). It has been shown that the PIF and the EPF capture well the eroded areas on the leading, center and trailing edge regions compared to those of the VIF. Therefore, the newly proposed EPF, based on both the temporal pressure variation and the cavitation volume, has been a reliable and powerful method for predicting erosion around hydrofoils.

Facing the complexity of identifying the erosion cause, we have adopted several hypotheses, inspired by previous publications, to estimate the impact pressure on the solid wall and its temporal evolution. We have varied the degree of proximity of micro-bubbles to the wall to choose either the shock wave or the micro-jet to estimate the impact pressure. We can conclude that:

- The used cavitation model can detect pressure waves in the vicinity of the wall, which justifies the use of the Rayleigh model to estimate the shock wave.

- For the shock wave case, the assumptions adopted such as the neglect of viscosity, surface tension and gas content, as well as the bubble shape, have directly affected the impact pressure, producing an overestimation of its amplitude.

- The Rayleigh model has only been valid for spherical collapses. Indeed, when $\gamma \leq 3$, the bubble is strongly deformed and the Rayleigh model is only applicable for very limited cases.

- Faced with all these constraints, the Rayleigh model has shown a lack of reliability concerning the micro-jet model, so it can therefore only be used for very limited applications where the shape of the bubbles is spherical, for a distance from the wall greater than $\gamma > 3$ and with a compressible solver. Hence, the performed calculations have responded more to the probability of the presence of a micro-jet than to the presence of a shock wave.

REFERENCES

Ait Bouziad, Y. (2006). *Physical modelling of leading edge cavitation: computational methodologies and application to hydraulic machinery*, Ph.D. Thesis, Lausanne, EPFL.

Arabnejad, M H., A. Amini, R. Bensow and M. Farhat (2018). Experimental and Numerical Investigation of the Cavitating Flows over a Modified NACA0009 Foil, In *proceedings of the 10th. International Symposium on Cavitation (CAV2018)*, Baltimore, Maryland, USA.

Arabnejad, M. H., A. Amini, M. Farhat and R. E. Bensow (2020a). Hydrodynamic mechanisms of aggressive collapse events in leading edge cavitation, *Journal of Hydrodynamics* 32(1), 6–19.

Arabnejad, M. H., U. Svennberg and R. E. Bensow, (2020b). Numerical assessment of cavitation erosion risk using incompressible simulation of cavitating flows, *Wear*, 464-465.

Bark, G., N. Berchiche and M. Grekula (2004). *Application of principles for observation and analysis of eroding cavitation, the erocav observation handbook*. EROCAV Report, Dept. of Naval Architecture, Chalmers University of Technology, Göteborg, Sweden.

Bensow, R. and G. Bark (2010). Implicit LES Predictions of the Cavitating Flow on a Propeller, *Journal of Fluids Engineering* 132 (4), 041302.

Blume, M. and R. Skoda (2019). 3d flow simulation of a circular leading edge hydrofoil and assessment of cavitation erosion by the statistical evaluation of void collapses and cavitation structures, *Wear* 428, 457–469.

Cheng, H. Y., X. R. Bai, X. P. Long, B. Ji, X. X. Peng and M. Farhat, (2020). Large eddy simulation of the tip-leakage cavitating flow with an insight on how cavitation influences vorticity and turbulence, *Applied Mathematical Modelling* 77, 788–809.

Dular, M. and O. Coutier-Delgosha (2009) Numerical modelling of cavitation erosion, *International Journal for Numerical Methods in Fluids* 61, 1388–1410.

Fortes Patella, R. and J. L. Reboud (1998) A New Approach to Evaluate the Cavitation Erosion Power, *Journal of Fluids Engineering* 120(2), 335–344.

Fortes-Patella, R., A. Archer and C. Flageul (2012). Numerical and experimental investigations on cavitation erosion, In *IOP Conference Series: Earth and Environmental Science* 15, 022013. IOP Publishing.

Franc J. P. and J. M. Michel (2004) *Fundamentals of Cavitation*, Kluwer.

Ji, B., L. Xianwu, A. Roger and W. Yulin (2014). Numerical simulation of three dimensional cavitation shedding dynamics with special emphasis on cavitation–vortex interaction, *Ocean Engineering* 87, 64–77.

Kanfoudi, H. (2012). *Modélisation de la cavitation dans un écoulement turbulent*, Ph. D. Thesis, University of Tunis El manar, ENIT.

Kanfoudi, H., G. Bellakhal, M. Ennouri, A. Bel Hadj Taher and R. Zgolli (2017). Numerical Analysis of the Turbulent Flow Structure Induced by the Cavitation Shedding using LES, *Journal of Applied Fluid Mechanics* 10

(3), 933-946.

Koukouvinis, P., G. Bergeles and M. Gavaises (2015). A cavitation aggressiveness index within the Reynolds averaged Navier Stokes methodology for cavitating flows, *Journal of Hydrodynamics* 27(4), 579–586.

Koukouvinis, P., N. Mitroglou, M. Gavaises, M. Lorenzi and M. Santini (2017). Quantitative predictions of cavitation presence and erosion-prone locations in a high-pressure cavitation test rig, Journal of Fluid Mechanics, 819, 21–57.

Krumenacker, L., R. Fortes-Patella and A. Archer (2014). Numerical estimation of cavitation intensity, In *IOP Conference Series: Earth and Environmental Science* 22, 052014.

Lei, T., C. Huai-yu, J. Bin and P. Xiao-xing (2021). Numerical assessment of the erosion risk for cavitating twisted hydrofoil by three methods, *Journal of Hydrodynamics* 33(4): 698-711.

Li, S., R. Han, A. M. Zhang and Q. X. Wang (2016). Analysis of pressure field generated by a collapsing bubble, *Ocean Engineering* 117, 22-38.

Li, Z. (2012). *Assessment of Cavitation Erosion with a Multiphase Reynolds-Averaged Navier-Stokes Method*, Ph.D. Thesis, Delft University of Technology.

Li, Z., M. Pourquie and T. van Terwisga (2014). Assessment of cavitation erosion with a urans method, *Journal of Fluids Engineering* 136(4), 041101.

Liang, W., T. Chen and G. Wang (2020). Investigation of unsteady liquid nitrogen cavitating flows with special emphasis on the vortex structures using mode decomposition methods, *International Journal of Heat and Mass Transfer* 157: 119880.

Lush, P. A. (1983). Impact of a liquid mass on a perfectly plastic solid. *Journal of Fluid Mechanics* 135, 373-387.

Menter, F. R. (1994). Two-Equation Eddy Viscosity Turbulence Models for Engineering Applications. *AIAA Journal* 32(8), 1598–1605.

Mihatsch, M., S. Schmidt and N. Adams (2015). Cavitation erosion prediction based on analysis of flow dynamics and impact load spectra, *Physics of Fluids* 27(10), 2015, 103302.

Nicoud, F. and F. Ducros (1999). Subgrid-scale stress modelling based on the square of the velocity gradient tensor, *Flow Turbulence and Combustion* 62(3): 183-200.

Ochiai, N., Y. Iga, M. Nohmi and T. Ikohagi (2013). Study of quantitative numerical prediction of cavitation erosion in cavitating flow, *Journal of Fluids Engineering* 135(1), 2013, 011302.

Peters, A. and O. El Moctar (2020). Numerical assessment of cavitation-induced erosion using a multi-scale euler–lagrange method, *Journal of Fluid Mechanics* 894, 1-54.

Peters, A., H. Sagar, U. Lantermann and O. El Moctar (2015). Numerical modelling and prediction of cavitation erosion, *Wear* 338–339, 189-201.

Peters, A., U. Lantermann and O. El Moctar (2018). Numerical prediction of cavitation erosion on a ship propeller in model-and full-scale, *Wear* 408, 1–12.

Plesset, M. S. and R. B. Chapman (1970) Collapse of an initially spherical vapor cavity in the neighborhood of a solid boundary, 85-49, California Institute of Technology.

Rayleigh, L. (1917). On the Pressure Developped in a Liquid During Collapse of a Spherical Cavity, *Philosophical Magazine* 34, 94-98.

Smagorinsky, J. (1963). General circulation experiments with the primitive equations, *Monthly Weather Review* 91: 99-164.

Tomita, Y. and A. Shima (1986). Mechanisms of impulsive pressure generation and damage pit formation by bubble collapse, *J. of Fluid Mech.* 169, 535-564.

Usta, O. and E. Korkut (2019). Prediction of cavitation development and cavitation erosion on hydrofoils and propellers by Detached Eddy Simulation, *Ocean Engineering* 191, 106512.

Van Terwisga, T., P. A. Fitzsimmons, Z. Li and E. J. Foeth (2009) Cavitation erosion - A review of physical mechanisms and erosion risk models, *Proceeding of the 7th International Symposium on Cavitation, CAV2009*, Delft University of Technology.

Vogel, A. and W. Lauterborn (1988). Acoustic transient generation by laser-produced cavitation bubbles near solid boundaries, *The Journal of the Acoustical Society of America* 84(2), 719–731.

Ye, W., Z. Zhu and Z. Qian (2020) Numerical analysis of unstable turbulent flows in a centrifugal pump impeller considering the curvature and rotation effect. *Journal of Mechanical Science and Technology* 34(7): 2869-2881.

Yuan, W., J. Sauer and G. H. Schnerr (2001). Modelling Annual Conference on Liquid atomization and spray and computation of unsteady cavitation flows in systems (ILASS-Europe 1994), paper VI-13 (Institute injection nozzles. *Mécanique & Industries* 2, 383–394.